J Mater Sci (2017) 52:2694–2704

Structural and multiferroic properties of $Bi_{0.92-x}Ho_{0.08}Sr_xFe_{0.97}Mn_{0.03}O_3$ thin films

Guoqiang Tan[1,*], Wei Yang[1,*], Wei Ye[1], Zhongwei Yue[1], Huijun Ren[1], and Ao Xia[1]

[1] School of Materials Science and Engineering, Shaanxi University of Science and Technology, Xi'an 710021, China

Received: 22 August 2016
Accepted: 2 November 2016
Published online: 9 November 2016

ABSTRACT

The $Bi_{0.92-x}Ho_{0.08}Sr_xFe_{0.97}Mn_{0.03}O_3$(BHSr$_x$FMO) thin films were deposited on FTO/glass substrates by the sol–gel method. The structure, surface morphologies, and electric properties of the thin films were investigated. The results show that the structure of BHSr$_x$FMO thin films transformed from rhombohedral *R3c:H* to rhombohedral *R3m:R* when doped with the Sr^{2+} ions. When the ferroelectric domain structure of the BHSr$_x$FMO(x = 0.00–0.04) thin films is converted from ferroelectric phase and antiferroelectric phase to ferroelectric phase, the coercive field (E_c) increased. This change occurs when the defect dipole of $(Sr'_{Bi} - V_O^{\cdot\cdot})^{\cdot}$ of BHSr$_x$FMO thin films increased, which clamps the domain wall motion and changes the directions of spontaneous polarization. In an electric field of 536 kV/cm, the $2P_r$ and $2E_c$ of BHSr$_3$FMO thin film are 81.9 μC/cm^2 and 524 kV/cm, respectively. In the magnetic field of 8000 Oe, the magnetization of the BHSr$_3$FMO thin film is 8.34 emu/cm^3. The BHSr$_3$FMO thin film shows the great multiferroic properties, which are mainly connected with the rhombohedral structure of *R3c:H* (51%)/*R3m:R*(49%) space groups at morphotropic phase boundary.

Introduction

$BiFeO_3$(BFO), one of the single-phase multiferroic materials, has both ferroelectric and ferromagnetic properties at room temperature (T_C = 1103 K, T_N = 640 K), and will produce a synergistic effect coupling between ferroelectric and ferromagnetic (magnetic coupling effect). BFO has the wide application prospect in the multistate memory, magnetic sensors, spintronic devices, and other fields [1]; hence it has attracted wide attention and research.

However, the volatilization of the Bi^{3+} of BFO and the valence states change of Fe will produce Fe^{2+} ions and oxygen vacancies. Therefore, BFO thin films have large leakage current and an unsaturated hysteresis loop in the applied electric field, and the ferroelectric property is poor. In addition, The pure BFO shows weak ferromagnetism due to the antiferromagnetic spin structure; hence the magnetoelectric coupling of the pure BFO is low and does not satisfy the practical application needs [2]. In order to improve the multiferroic properties of BFO thin films, an ion doping can be carried out. The research shows that an ion doping can reduce the leakage current, improve the properties of ferroelectric, but the ferromagnetic properties are not been increased obviously.

Address correspondence to E-mail: tan3114@163.com; 397830680@163.com

DOI 10.1007/s10853-016-0560-x

Our research group has done a lot of research work about ions doping on BFO thin films. For example, Liu et al. [3] have observed that Sr^{2+} ions doping could improve the ferroelectric property ($2P_r \sim 173.43\ \mu C/cm^2$), while the ferromagnetism did not increase significantly ($M_s \sim 2.3\ emu/cm^3$) in $Bi_{0.89-x}Sm_{0.11}Sr_xFe_{0.94}(Mn_{0.04}Cr_{0.02})O_3$ films. Meanwhile, Ye et al. [4] prepared BFO thin films of Ho and Mn co-doping, the ferroelectric improved ($2P_r \sim 231.4\ \mu C/cm^2$), but the ferromagnetic did not increase significantly ($M_s \sim 2.74\ emu/cm^3$). More importantly, Dong et al. [5] have founded that the leakage current of the Tb, Mn, and Cr co-doped BFO thin films decreased, and the multiferroic properties improved ($2P_r \sim 239.6\ \mu C/cm^2$, $M_s \sim 10.5\ emu/cm^3$).

According to the above research, the $Bi_{0.92-x}Ho_{0.08}Sr_xFe_{0.97}Mn_{0.03}O_3$ (BHSr$_x$FMO, $x = 0.01$–0.04) thin films were prepared with the sol–gel method in this work, and we hope this will further increase the ferromagnetic property of BFO thin films.

Experimental procedure

$Bi_{0.92-x}Ho_{0.08}Sr_xFe_{0.97}Mn_{0.03}O_3$ (BHSr$_x$FMO, $x = 0.01$–0.04) thin films were fabricated on FTO (Fluorine doped tin oxide)/glass substrates using the sol–gel method. $Bi_{0.91}Ho_{0.08}Sr_{0.01}Fe_{0.97}Mn_{0.03}O_3$, $Bi_{0.90}Ho_{0.08}Sr_{0.02}Fe_{0.97}Mn_{0.03}O_3$, $Bi_{0.89}Ho_{0.08}Sr_{0.03}Fe_{0.97}Mn_{0.03}O_3$, and $Bi_{0.92-x}Ho_{0.08}Sr_{0.04}Fe_{0.97}Mn_{0.03}O_3$ thin films (hereinafter referred to as BHSr$_1$FMO, BHSr$_2$FMO, BHSr$_3$FMO, and BHSr$_4$FMO thin films, respectively) were successfully obtained. As raw materials, bismuth nitrate pentahydrate ($Bi(NO_3)_3{\cdot}5H_2O$, 5 mol% of excess Bi), $Sr(NO_3)_2$, $Ho(NO_3)_3{\cdot}6H_2O$, iron nitrate nonahydrate ($Fe(NO_3)_3{\cdot}9H_2O$), manganese acetate tetrahydrate ($C_4H_6MnO_4{\cdot}4H_2O$), were mixed together with the atomic ratio of 0.92-x:0.08:x:0.97:0.03. Then raw materials were dissolved in the 2-methoxyethanol and acetic anhydride solvents, in which the volume ratio of 2-methoxyethanol and acetic anhydride was 3:1. The concentration of Fe^{3+} ion was 0.3 mol/L in the precursor solutions. Next, the solutions were stirred at room temperature for 2 h to obtain the homogeneous precursor solutions. The precursor solutions were deposited on FTO/glass substrates using a spin-coating method at a constant spinning rate of 4000 rpm for 15 s. After spin-coating, the deposited wet films were preheated at 473 K on a hot plate for 8 min and then the dried films were inserted into a furnace at 823 K under an air atmosphere for crystallization. These processes were repeated 15 times so as to obtain the desired film thickness. In order to measure the electrical properties, Au top electrodes (with the areas of 0.003 mm^2) were deposited on the top surface of the thin films by ions sputtering through a metal shadow mask. After annealing at 558 K for 30 min, the electrodes could completely contact with the film.

An D/max-2200 X-ray diffractometer (XRD) by Japan Rigaku Company was used to identify the phase composition and crystal structure of the thin films. Raman spectroscopy measurements were performed by a British Renishaw inVia micro Raman spectrometer with an Ar ion laser excitation at 532 nm. A field emission scanning electron microscopy (FE-SEM, S4800, Hitachi) was used to observe the surface morphologies and interface contact of the films. The surface element composition and ion valence state of the samples were analyzed using an XPS of the XSAM800 spectrometer with Kratos. The leakage current densities of the films were measured by an Agilent E4980A. The electric hysteresis loops of the films were measured by a Radiant Multiferroic, and the magnetic properties of the films were analyzed using an MPMS-XL-7 superconducting quantum interference magnetic measuring system at room temperature.

Results and discussion

Structural characterization

Figure 1 is the XRD patterns of the pure BFO and BHSr$_x$FMO thin films. The diffraction peaks of BFO and BHFMO thin films are consistent with the Standard Card of PDF (JCPDS No. 86-1518), which has distorted the rhombohedral perovskite structure, and the space lattices are *R3c:H* (161). There is a peak at the 2θ of 24°in the BHFMO thin film, which is the impurity phase of $Bi_2Fe_4O_9$ [4]. The diffraction peaks of BHSr$_x$FMO films are consistent with the Standard Card of PDF (JCPDS No. 74-2016); space lattices are *R3m*(160); and there are no impurity phases. Figure 1b shows the magnification of XRD patterns at the 2θ range of 30°–34°. The (104) peak of the BFO film is stronger than (110) peak. However, the intensity of (104) peak is weakened with Sr, Ho, and

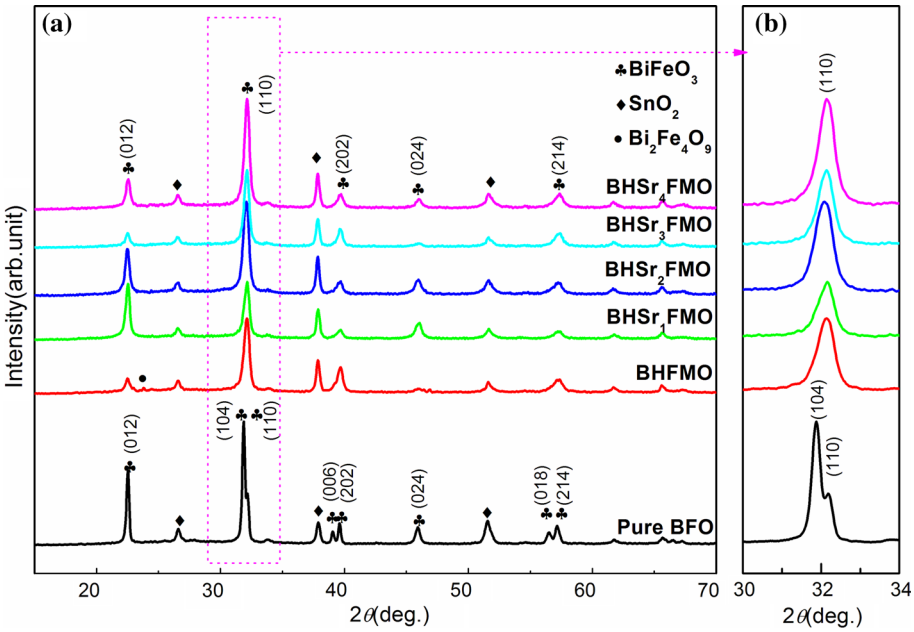

Figure 1 **a** XRD patterns of pure BFO and $BHSr_xFMO$ thin films; **b** the magnified XRD patterns at the 2θ range of 30–34°.

Mn co-doping, and later on the (104) peak and (110) peak are merged to a broad single peak. Compared with BHFMO and $BHSr_xFMO$, we can find that the (110) peak of $BHSr_xFMO$ becomes wider than BHFMO, and the intensity increases when the amount of Sr^{2+} doping is more than 2%. This may be because Sr^{2+} doping makes the crystallinity of BHFMO film become better, and the grain sizes increases [6]. The changes of $BHSr_xFMO$ thin film peaks are due to the ionic radius of Sr^{2+}(1.12 Å) large than that of Bi^{3+}(1.03 Å), and the different ionic radii of doping leads to the distorted structure of the films [7].

In order to further analyze the effects of Sr^{2+} doping on the crystal structure of $BHSr_xFMO$ thin films, Rietveld refinement of XRD patterns (for all samples) have been preformed using the Maud program [8], as shown in Fig. 2 (the illustrations are structure models). The crystal structure parameters obtained from the Rietveld refinement of the XRD patterns are listed in Table 1. The refinement results agree with the experimental data, and the error factors (R_w) are below 10.50%. According to the refinement results, the pure BFO film belongs to rhombohedral structure, *R3c:H* space group. BHFMO film belongs to rhombohedral structure, the *R3c:H* (73%) and *R3m:R* (27%); space group exhibits two kinds of coexistence [4]. From Table 1, we can also see that $BHSr_xFMO$ thin films belong to rhombohedral structure, *R3c:H* and *R3m:R* space groups. With the increased amount of Sr^{2+} doping, the proportions of *R3m:R* space groups are 37, 37, 49, and 36%, respectively. The lattice parameter (a) of *R3m:R* space group decreases from 3.954 to 3.797 Å, and the cell volume decreases from 61.811 to 51.362 $Å^3$ with the increase of Sr^{2+} doping. It indicates that the space group of $BHSr_xFMO$ transforms from *R3c:H* to *R3m:R* with the increase of Sr^{2+} doping, and the structural distortion degree increases. When the amount of Sr^{2+} doping is 0.03, the lattice distortion is the most obvious.

As we all know, the structure transformation of films can also be reflected by Raman spectroscopy. Figure 3a shows Raman spectra of the pure BFO and $BHSr_xFMO$ thin films at room temperature, and each Raman active modes are obtained by decomposing the fitted curves into individual Lorentzian components. According to the group theory, the rhombohedral *R3c* structure of BFO has 13 Raman active modes ($\Gamma = 4A_1 + 9E$) [9]. In this experiment, the $BHSr_xFMO$ ($x = 0.01$–0.04) films have 8 active modes, and A_1-1, A_1-2, and A_1-3 active modes of $BHSr_1FMO$ film are located at 144, 175, and 221 cm^{-1}, and the E modes of $BHSr_1FMO$ film are located at 262, 369, 478, 523, and 611 cm^{-1}, respectively. In addition, two-phonon modes are also observed around 900–1300 cm^{-1} in Fig. 3b [10]. The three different two-phonon Raman spectra of Pure BFO are $2A_4$(960 cm^{-1}), $2E_8$(1100 cm^{-1}), and $2E_9$(1240 cm^{-1}), but the intensities of two-phonon modes are

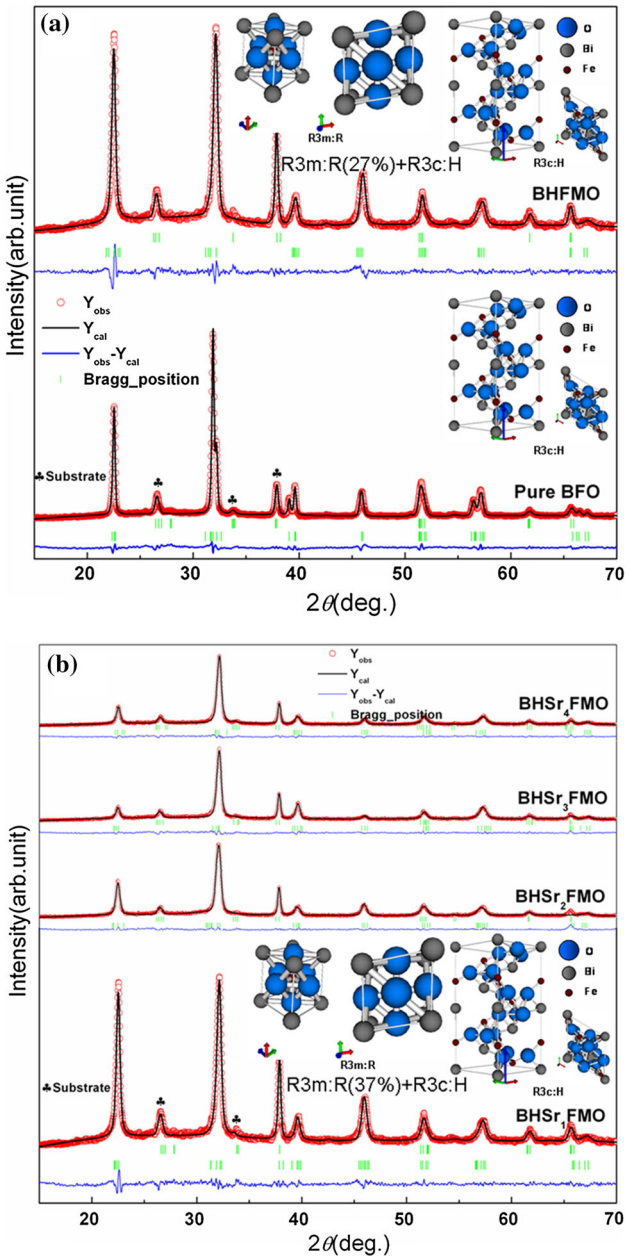

Figure 2 **a** Rietveld-refined XRD patterns of the pure BFO and BHFMO thin films, **b** Rietveld-refined XRD patterns of the $BHSr_xFMO$ thin films.

significantly decreased with doping Sr^{2+}, Ho^{3+}, and Mn^{2+} ions. Compared with the Raman active modes between BFO and BHFMO films, the following two conclusions can be obtained. On the one hand, it is known that the low frequency A modes are related to the Bi–O vibration and the high frequency E modes are related to the Fe–O vibration [11, 12]; On the other hand, the low frequency of A_1-1, A_1-2, A_1-3 active modes have been merged, and the intensity of the E mode is increased at 621 cm^{-1}. It indicates that Ho^{3+} and Mn^{2+} ions are doped into the BFO crystal lattice, which makes the Bi–O and Fe–O bond active modes change significantly [4]. Compared with Raman active modes of BHFMO and $BHSr_xFMO$ ($x = 0.01$–0.04) films, we can see that the intensities of A_1-1, A_1-2, A_1-3 active modes decrease at the low frequency, and E mode (621 cm^{-1}) shifts to the high frequency. This shows that Sr^{2+} ion is doped into the BFO lattice, which leads to the distortion of the structure of BHFMO film. The analyses of the Raman spectra support the XRD patterns analysis conclusion, and Sr^{2+} doping can cause the significant distortion of the structure of BHFMO thin film.

The FE-SEM images of the surface and the cross-section micrographs of the pure BFO and $BHSr_xFMO$ thin films are shown in Fig. 4. Figure 4a shows the surface and the cross-section micrographs of the pure BFO film, which has the large grain size of about 150 nm, and the grains boundary are obvious. From the cross section, it can be seen that the thickness of the films is about 500 nm. Figure 4b shows the surface and the cross-section micrographs of BHFMO thin film, and the grain size is decreased obviously. This is because the doping ions (Ho^{3+} and Mn^{2+}) act as nucleation centers in the BHFMO thin film, and the nucleation rate increases; this results in the decrease of the grain growth rate and the grain size [4]. The effects of ion doping on the grain size of BFO have also been reported in the BFO films doped with other ions [13, 14]. Figure 4c–f shows the surface and the cross-section micrographs of $BHSr_1FMO$, $BHSr_2FMO$, $BHSr_3FMO$, and $BHSr_4FMO$ thin films, respectively. With the increased amount of Sr^{2+} doping, the grain size increases. It further indicates that due to the Sr^{2+} doping, the grain size of $BHSr_xFMO$ thin film increases in the XRD patterns. The abnormal growth of some grains causes the distribution of grain size not to be uniform, as shown in Fig. 4e. The grain size of the $BHSr_3FMO$ film is at the range of 50–120 nm. Meanwhile, the inset of Fig. 4e is the cross-section micrographs of the $BHSr_3FMO$ thin film. The thickness of the film is 550 nm, and the abnormal growth of grains leads to the surface of the film not to be smooth, so the uneven distribution of the particle size will cause the lattice strain [15]. In addition, Sr^{2+} doping leads to the film surface not to be smooth, which may affect the leakage current and ferroelectric properties [16].

Table 1 Details of the Rietveld-refined structural parameters of the pure BFO and $BHSr_xFMO$ thin films simulated based on the measured XRD patterns

Samples	Crystal structure	Space group	Lattice parameters (Å, Å^3)	*R*-factors (%)
BFO	Rhombohedral structure	*R3c:H*	$a = 5.5797$ $c = 13.8741$ Volume = 374.07	$R_w = 10.14$ $R_{wnb} = 6.76$ $R_b = 7.28$
BHFMO	Rhombohedral structure	*R3c:H* *R3m:R*(27%)	$a = 5.5789$ $c = 13.8362$ Volume = 372.94 $a = 3.9540$ $\alpha = 89.5397°$ Volume = 61.811	$R_w = 8.480441$ $R_{wnb} = 6.5834394$ $R_b = 5.91236$
$BHSr_1FMO$	Rhombohedral structure	*R3c:H* *R3m:R*(37%)	$a = 5.5884$ $c = 13.6345$ Volume = 367.5 $a = 3.9587$ $\alpha = 89.8190°$ Volume = 62.037	$R_w = 10.422142$ $R_{wnb} = 10.134931$ $R_b = 6.8835807$
$BHSr_2FMO$	Rhombohedral structure	*R3c:H* *R3m:R*(37%)	$a = 5.5882$ $c = 13.6360$ Volume = 368.78 $a = 3.8008$ $\alpha = 77.4140°$ Volume = 51.456	$R_w = 7.437629$ $R_{wnb} = 7.2740874$ $R_b = 5.669479$
$BHSr_3FMO$	Rhombohedral structure	*R3c:H* *R3m:R*(49%)	$a = 5.5826$ $c = 13.6137$ Volume = 367.43 $a = 3.7998$ $\alpha = 77.6299°$ Volume = 51.524	$R_w = 8.437053$ $R_{wnb} = 6.927182$ $R_b = 6.5886555$
$BHSr_4FMO$	Rhombohedral structure	*R3c:H* *R3m:R*(36%)	$a = 5.5755$ $c = 13.6054$ Volume = 366.28	$R_w = 8.856583$ $R_{wnb} = 5.147855$ $R_b = 6.232$

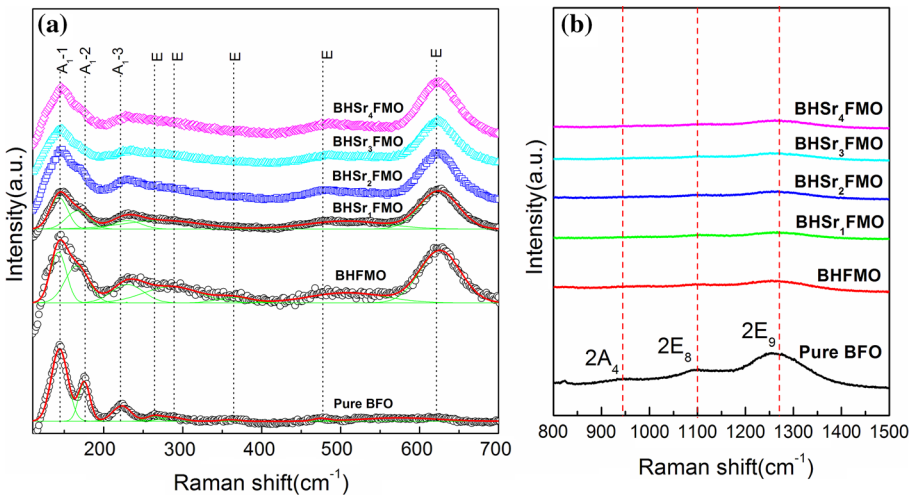

Figure 3 Raman spectra of the pure BFO and $BHSr_xFMO$ thin films.

As we all know, the main factors affecting the leakage current of BFO thin films include the fluctuation of the valence state between Fe^{3+} and Fe^{2+} ions and the oxygen vacancies. In addition, the valence state of Mn ions may be changed, so it also needs to make the analysis of Mn valence. The chemical

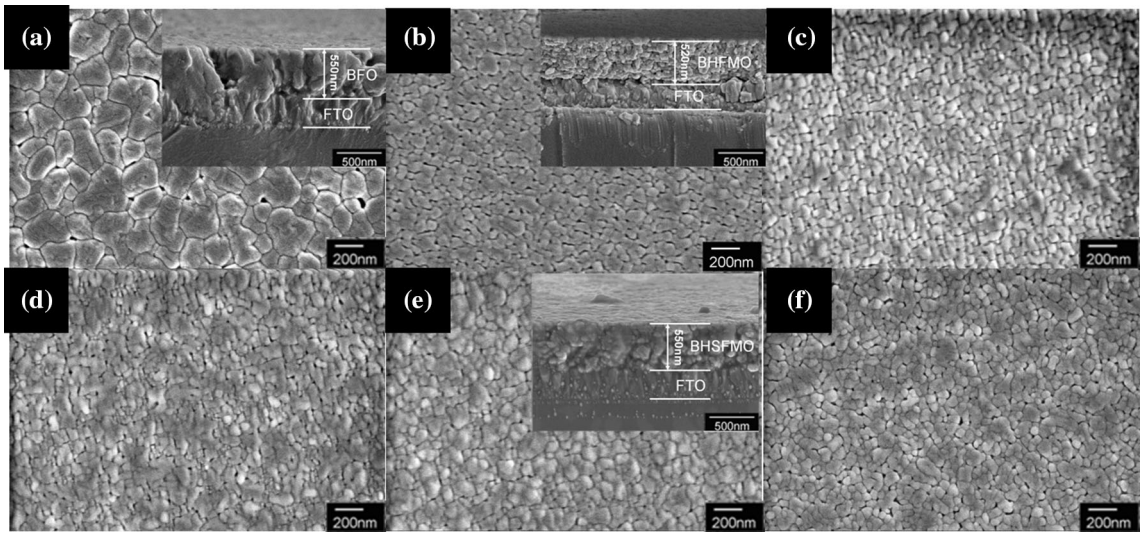

Figure 4 The FE-SEM images of the surface and the cross-section micrographs of the pure BFO and $BHSr_xFMO$ thin films, **a** pure BFO (illustration of the cross-section images), **b** BHFMO, **c** $BHSr_1FMO$, **d** $BHSr_2FMO$, **e** $BHSr_3FMO$, **f** $BHSr_4FMO$.

valence states of Fe 2p, Mn 2p, and O 1 s are analyzed by XPS, as shown in Fig. 5. By fitting the Fe $2p_{3/2}$ peaks of all the thin films, as shown in Fig. 5a, the results show that all the thin films contain both Fe^{2+} and Fe^{3+}. The ratios of Fe^{2+} ions of BFO and $BHSr_x$-FMO ($x = 0.00$–0.04) thin films are 44.80, 27.52, 19.82, 16.20, 14.74, and 13.86%, respectively, and the amount of Fe^{2+} ions decreases with the increase of Sr^{2+} amount. The valence state of Fe is very sensitive to the oxygen vacancies. In order to maintain the electrical neutrality, the formation of Fe^{2+} ions is bound to be accompanied by the oxygen vacancies, as shown in Eqs. (1) [17] and (2). The chemical valence states of Mn in the films are fitted by XPS spectra, as shown in Fig. 5b. The results indicate that there are Mn^{2+} and Mn^{3+} ions. The ratios of Mn^{2+} ions of $BHSr_xFMO$ ($x = 0.00$–0.04) thin films are 55.32, 59.07, 50.41, 51.36, 47.43%, respectively, and the valence fluctuation may occur as shown in the following Eq. (3).

With the increase of Sr^{2+} doping, the Mn^{2+} ions of $BHSr_1FMO$ thin films decrease because Sr^{2+} and Ho^{3+} ions doping promotes the binding of Mn^{2+} and oxygen vacancies. The equilibrium is shifted to the right, as shown in Eq. (4) [18]. Figure 5c shows the O 1 s of XPS spectra of the pure BFO and $BHSr_xFMO$ ($x = 0.00$–0.04) thin films. The O 1 s track contains two peaks, with peak (O_L) of low binding energy associated with BFO lattice oxygen, and peak (O_H) of high binding energy associated with oxygen vacancies [19]. The ratios of O_H of BFO and $BHSr_xFMO$($x = 0.00$–0.04) thin films are 20.59, 13.66, 14.05, 11.56, 12.92, 10.08%, respectively. The oxygen vacancies of BHFMO thin film decrease, because the Ho^{3+} ions substituting Bi^{3+} ions can decrease the volatilization of Bi^{3+} ions and lower the concentration of oxygen vacancies [20]. The amount of oxygen vacancies decreases with the Sr^{2+} doping, which is consistent with the results of the Fe $2p_{3/2}$ peaks. This is because Sr^{2+} and Ho^{2+} ions substitute Bi^{3+} ions of $BHSr_xFMO$ thin films and the internal charge of the film reaches a state of equilibrium, which will produce a part of the oxygen vacancies. The component defect equation is as shown in Eq. (5). However, the oxygen vacancies of $BHSr_3FMO$ thin films increase, which may be related to the structural distortion and the abnormal growth of some grains. According to the results of XPS spectra analyses, a certain amount of doping Sr^{2+} ions reduces the Fe^{2+} ions and oxygen vacancies, but Mn^{3+} ions increase, which shows that the valence state fluctuation of $BHSr_xFMO$ films is more obvious with doping Sr^{2+} ions. Accordingly, the decrease of Fe^{2+}, Mn^{2+}, and oxygen vacancies lead to the decrease of defect dipole of $(Fe'_{Fe} - V_O^{\cdot\cdot})^{\cdot}$, so the oxygen vacancies of $BHSr_1FMO$ film are increased. In addition, the defect dipole of $(Sr'_{Bi} - V_O^{\cdot\cdot})^{\cdot}$ increases with the increase of doping Sr^{2+} ions, and thus the oxygen vacancies decrease [21]. The results may have a significant impact on the electrical properties of $BHSr_xFMO$ thin films.The defect chemical equations of BFO:

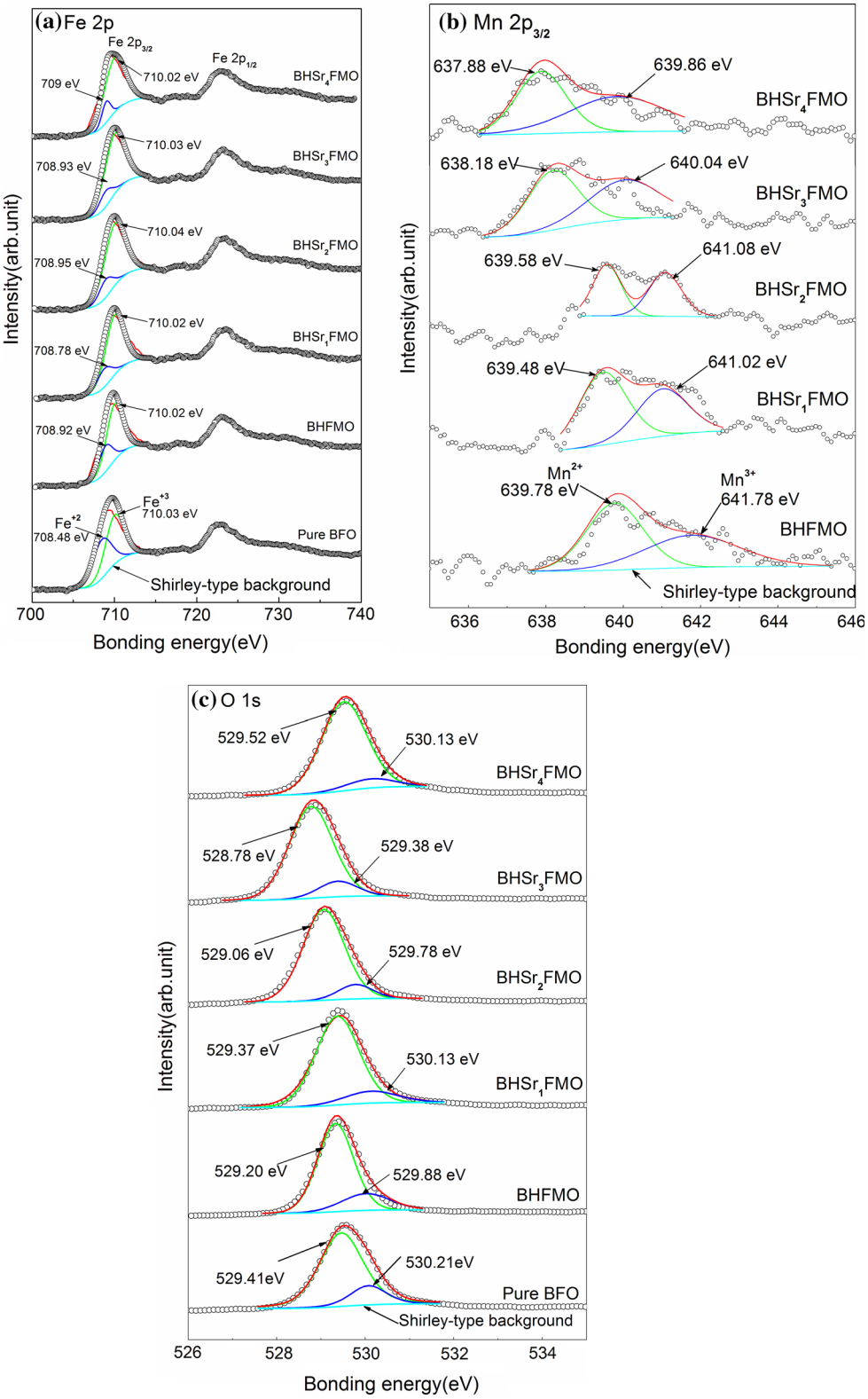

Figure 5 XPS spectra of **a** Fe 2p, **b** Mn 2p, and **c** O1 s of the pure BFO and $BHSr_xFMO$ thin films.

$$2Fe_{Fe} + O_O \rightarrow 2Fe'_{Fe} + V_O^{\cdot\cdot} + 1/2O_2 \quad (1)$$

$$2Bi_{Bi} + 3O_O \rightarrow 2V'''_{Bi} + 3V_O^{\cdot\cdot} + Bi_2O_3 \quad (2)$$

The defect chemical equations of BHFMO:

$$Mn^{2+} + Fe^{3+} \rightarrow Mn^{3+} + Fe^{2+} \quad (3)$$

$$MnO \xrightarrow{Fe_2O_3} 2Mn'_{Fe} + V_O^{\cdot\cdot} + 2O_O^{\times} \quad (4)$$

The defect chemical equations of $BHSr_xFMO$:

$$2SrO \xrightarrow{Bi_2O_3} 2Sr'_{Bi} + V_O^{\cdot\cdot} + 2O_O^{\times} \quad (5)$$

Properties of thin films

Figure 6 shows the leakage current density of $BHSr_xFMO$ thin films at room temperature. The leakage current density of BHFMO thin film is 6.25×10^{-6} A/cm^2 at 300 kV/cm. It can be seen that the leakage current density of thin films decreases with doping Sr^{2+} ions, and the leakage current densities of $BHSr_xFMO$ ($x = 0.01$–0.04) thin films are 1.8×10^{-5}, 1.39×10^{-6}, 1.74×10^{-6}, 1.15×10^{-6} A/cm^2, respectively, at 300 kV/cm. The leakage current of $BHSr_1FMO$ thin film increases, which is due to the increase of oxygen vacancies and the decrease of the defect dipoles of $(Sr'_{Bi} - V_O^{\cdot\cdot})^{\cdot}$. Generally, the leakage current density decreases with the increase of the amount of doping Sr^{2+} ions. Combining the XPS analysis results shows that Sr^{2+} and Ho^{3+} ions substituting Bi^{3+} ions can decrease the oxygen vacancies, resulting in the decrease of leakage current density [22]. This is different from the reports of Sr^{2+}-doped BFO thin films [23].

Figure 7 shows the ferroelectric hysteresis loops (P–E) and the transient currents recorded curve (I–E) of the $BHSr_xFMO$ thin films measured at room temperature and 1 kHz. In an applied electric field of 536 kV/cm, the remnant polarization ($2P_r$) and coercive field ($2E_c$) of BHFMO thin film are 57.1 μC/cm^2 and 477 kV/cm, respectively. The P–E hysteresis

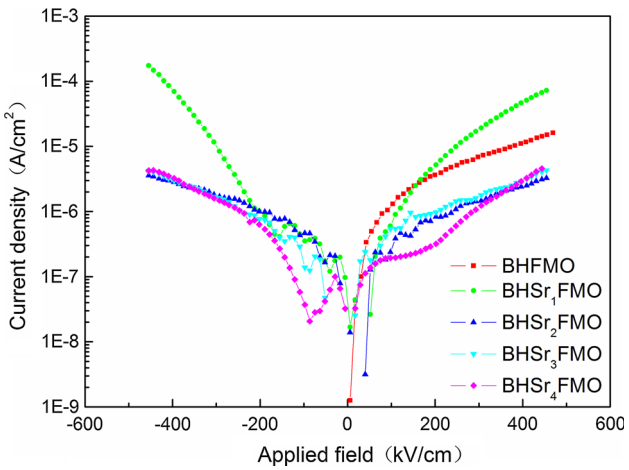

Figure 6 The Leakage current density of $BHSr_xFMO$ thin films at RT.

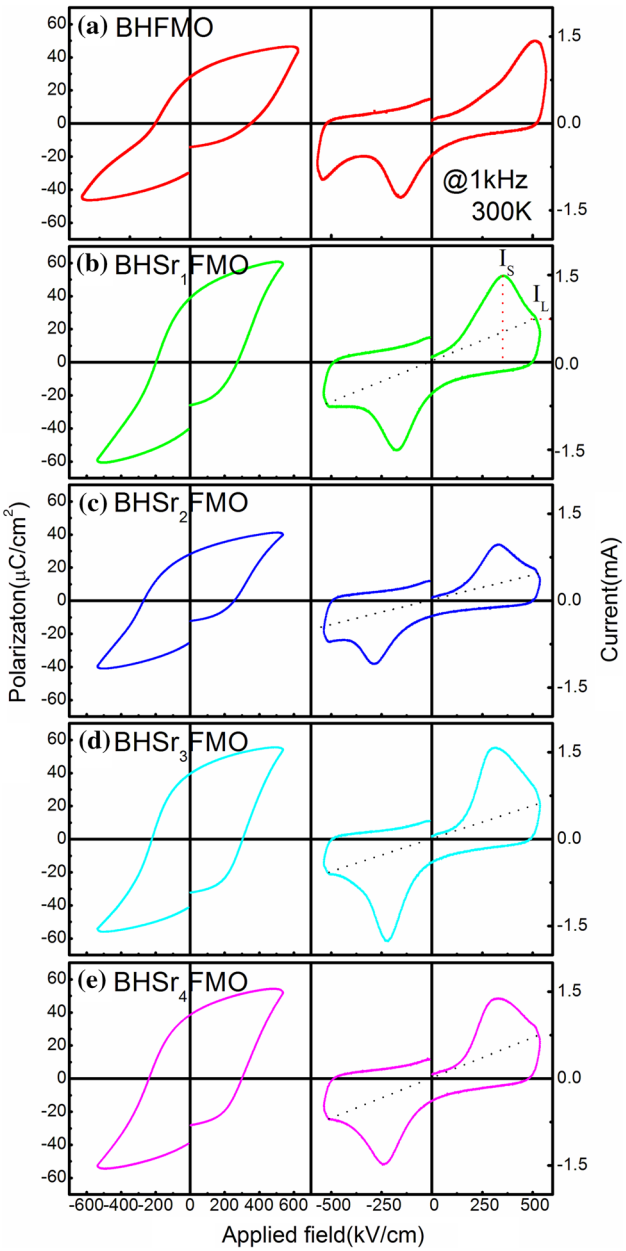

Figure 7 The ferroelectric hysteresis loops (P–E) and the transient currents recorded curves (I–E) of the $BHSr_xFMO$ thin films measured at 1 kHz.

loop of the BHFMO thin film is shrunk at the negative coercive field, which leads to the asymmetry of the coercive field. At the same time, the *I–E* curve has two peaks in the negative electric field, which is in line with the antiferroelectric, so the BHFMO thin film has ferroelectric phase and antiferroelectric phase. This is because the $(Fe'_{Fe} - V_O^{\cdot\cdot})^{\cdot}$ and $(Mn'_{Fe} - V_O^{\cdot\cdot})^{\cdot}$ defect dipoles are formed in the BHFMO film, which can make the ferroelectric domain difficult to switch and can cause the pinning effect on the domain wall, so make the ferroelectric domain difficult to switch [24]. The $2P_r$ and $2E_c$ of $BHSr_1FMO$ thin films are 80.1 μC/cm^2 and 473 kV/cm, respectively, and the antiferroelectric phase disappears, which is due to the decrease of the $(Fe'_{Fe} - V_O^{\cdot\cdot})^{\cdot}$ and $(Mn'_{Fe} - V_O^{\cdot\cdot})^{\cdot}$ defect dipoles with doping Sr^{2+} ions, the decrease of the pinning effect, and the ferroelectric domain easy to switch.

The $2P_r$ and $2E_c$ of $BHSr_xFMO$ ($x = 0.02$–0.04) thin films are 53.5, 81.9, 78.4 μC/cm^2 and 532, 524, 540 kV/cm, respectively. The $2E_c$ of $BHSr_x$-FMO($x = 0.01$–0.04) thin films is increased from 473 to 524 kV/cm. There are two reasons: on the one hand, the increase of the $2E_c$ is due to the increase of the defect dipole of $(Sr'_{Bi} - V_O^{\cdot\cdot})^{\cdot}$, which clamps the domain wall motion. On the other hand, the ferroelectric phase plays an important role in the spontaneous polarization directions. It is generally known that the polarization direction of *R3c:H* space group of BFO thin film is [111] [25]. Although the *R3c:H* and *R3m:R* space groups belong to the *3m* point group, the symmetric axis of *R3m:R* space group shifts.

The refinement results show that the α of the *R3c:H* space group is 90°, and the α of the *R3m:R* space group of $BHSr_xFMO$($x = 0.01$–0.04) thin films decreases from 89° to 77° (Table 1). Although the polarization direction of *R3m:R* space group of $BHSr_xFMO$ thin films is also [111], and the α of the *R3m:R* space group changes, which indicates that the polarization direction is changed, and the ferroelectric domain is difficult to switch, the $2E_c$ of $BHSr_x$FMO($x = 0.01$–0.04) thin films increases with the increase of the *R3m:R* space group.

The further analyses of the transient currents recorded curve show that the *I–E* curve consists of two parts. One part is that the ferroelectric domain inversion produces the real polarization current. The other part is that the leakage current causes the linear resistance of the interface between the thin film and

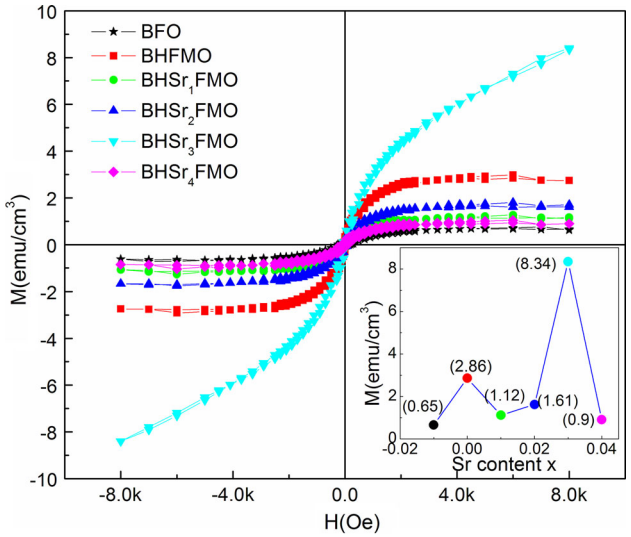

Figure 8 Magnetic hysteresis loops of the pure BFO and $BHSr_xFMO$ thin films at RT.

the electrode, which leads to the increase of the switching current and leakage current of all the films [26]. And the *I–E* curve shows that the switching current (I_S) and the leakage current (I_L) of $BHSr_xFMO$ ($x = 0.01$–0.04) thin films are 1.48, 0.97, 1.57, 1.37 mA and 0.75, 0.45, 0.65, 0.75 mA, respectively. The $BHSr_3FMO$ thin films show great ferroelectric properties, and the enhanced ferroelectric properties are mainly connected with the rhombohedral structure of *R3c:H* (51%)/*R3m:R*(49%) space groups at morphotropic phase boundary (MPB) [27].

Figure 8 shows the magnetic hysteresis loops (*M–H*) of the pure BFO and $BHSr_xFMO$ thin films at room temperature. In the magnetic field of 8.0 k Oe, BFO thin film shows the weak ferromagnetic property ($M_s = 0.65$ emu/cm^3), which is because of the presence of Fe^{3+}–O–Fe^{3+} bond in pure BFO and shows G-type antiferromagnetic ordering [28]. The saturation magnetization of BHFMO thin films increases ($M_s = 2.73$ emu/cm^3), which is due to the increase of the oxygen vacancies, and the spin bond angle of Fe^{3+}–O–Fe^{3+} tilt [29]. The saturation magnetizations (M_s) of $BHSr_xFMO$ ($x = 0.01$, 0.02, 0.04) thin films are 1.12, 1.61, and 0.9 emu/cm^3, respectively. However, the magnetization of the $BHSr_3FMO$ thin film is 8.34 emu/cm^3, and does not reach saturation in the magnetic field of 8.0 k Oe, which may be due to two reasons: On the one hand, according to the Rietveld results and the Raman spectra, it can be found that $BHSr_3FMO$ thin film belongs to rhombohedral

structure, *R3c:H*(51%)/*R3m:R*(49%) space groups, and it is similar to the morphotropic phase boundary (MPB). It is indicated that the structural transformation gives rise to the continuing collapse of the space-modulated spin structure, which will release more magnetic power [30]. And the high frequency *E* mode (621 cm^{-1}) of $BHSr_3FMO$ thin film is shifted to the high frequency, which shows that the change of the Fe–O bond of $BHSr_3FMO$ film will lead to the change of G-type antiferromagnetic ordering and the Fe^{3+}–O–Fe^{2+} bond angle, and the antiferromagnetic lattice of BFO tilts. Thus, the magnetic properties of the $BHSr_3FMO$ film can be improved [31]. Furthermore, for multiferroic-based BFO materials, the effect of grain size influences the magnetic properties (mainly for a nonmetric grain size): with dimension less than 62 nm, the probable modification of cycloid spin structure of $BiFeO_3$ can influence ferromagnetism [32]. The grain size of the $BHSr_3FMO$ film is in the range of 50–120 nm, and the abnormal growth of grains leads to different magnetic properties. On the other hand, combined with the leakage current and XPS analyses, the oxygen vacancies and Mn^{3+} ions of the $BHSr_3FMO$ thin film increase, which showed that the increase of oxygen vacancies makes the clusters of Fe^{3+}–O–Fe^{2+} tilt, and the different magnetic moments of Mn^{2+} ions and Fe^{3+} ions also restrain the spiral spin structure [33]. Generally, the magnetic properties of $BHSr_3FMO$ thin film can be improved by the increase of structural distortion and oxygen vacancies.

Conclusions

The $BHSr_xFMO$ thin films are deposited on FTO substrates by the sol–gel method. The structural analyses show that $BHSr_xFMO$ ($x = 0.01$–0.04) thin films belong to rhombohedral structure, the Sr^{2+} ions doping causes the space groups transition from *R3c:H* to *R3m:R*. The Fe^{2+} and oxygen vacancies decrease with doping Sr^{2+} ions, and the leakage current density of $BHSr_3FMO$ film is 1.74×10^{-6} A/cm^2 at 300 kV/cm. In an applied electric field of 536 kV/cm, the $2P_r$ and $2E_c$ of $BHSr_3$ FMO thin film are 81.9 μC/cm^2 and 524 kV/cm, respectively. The I–E curve of $BHSr_3FMO$ thin film shows that the I_S and the I_L are 1.57 and 0.65 mA, respectively. In the magnetic field of 8000 Oe, the magnetization of the $BHSr_3FMO$ thin film increases significantly ($M = 8.34$ emu/cm^3). The $BHSr_3FMO$ thin film shows the great multiferroic properties, which is mainly connected with the rhombohedral structure of *R3c:H* (51%)/*R3m:R*(49%) space groups at morphotropic phase boundary (MPB). It is believed that the multiferroic properties of $BHSr_xFMO$ thin films may have more potential applications in multiferroic microdevices and spintronic devices.

Acknowledgments

This work is supported by the Project of the National Natural Science Foundation of China (Grant No. 51372145), the Academic Leaders Funding Scheme of Shaanxi University of Science and Technology (2013XSD06), and the Graduate Innovation Fund of Shaanxi University of Science and Technology (SUST-A04).

References

[1] Fiebig M, Lottermoser T, Gottsev AV et al (2002) Observation of coupled magnetic and electric domains. Nat Mater 419:818–820

[2] Popov YF, Kadomtseva AM, Krotov SS et al (2001) Features of the magnetoelectric properties of $BiFeO_3$ in high magnetic fields. Low Temp Phys 27:478–479

[3] Liu W, Tan G, Xue X et al (2014) Structure and multiferroic properties of Sr substituted $Bi_{0.89-x}Sm_{0.11}Sr_xFe_{0.94}(Mn_{0.04}Cr_{0.02})O_3$ thin films. Ceram Int 40:13249–13256

[4] Ye W, Tann G, Dong G et al (2015) Improved multiferroic properties in (Ho, Mn) co-doped $BiFeO_3$ thin films prepared by chemical solution deposition. Ceram Int 41:4668–4674

[5] Dong G, Tan G, Luo Y et al (2014) A comparative investigation on structure and multiferroic properties of bismuth ferrite thin films by multielement co-doping. Mater Res Bull 60:596–603

[6] Bhushan B, Basumallick A, Vasanthacharya NY, Kumar S, Das D (2010) Sr induced modification of structural, optical and magnetic properties in $Bi_{1-x}Sr_xFeO_3$(x = 0, 0.01, 0.03, 0.05 and 0.07) multiferroic nanoparticles. Solid. State Sci 12:1063–1069

[7] Varshney D, Kumar A (1038) Structural, Raman and dielectric behavior in $Bi_{1-x}Sr_xFeO_3$ multiferroic. J Mol Struct 2013:242–249

[8] Simões AZ, Cavalcante LS, Moura F et al (2011) Structure, ferroelectric/magnetoelectric properties and leakage current density of $(Bi_{0.85}Nd_{0.15})FeO_3$ thin films. J Alloys Compd 509:5326–5335

[9] Kothari D (2008) Raman scattering study of polycrystalline magnetoelectric $BiFeO_3$. J Magn Magn Mater 320:548–552
[10] Ramirez MO, Krishnamurthi M, Denev S et al (2008) Two-phonon coupling to the antiferromagnetic phase transition in multiferroic $BiFeO_3$. Appl Phys Lett 92:022511
[11] Sati PC, Arora M, Chauhan S et al (2012) Structural, magnetic, and optical properties of Pr and Zr codoped $BiFeO_3$ multiferroic ceramics. J Appl Phys 112:094102
[12] Ramachandran B, Rao MSR (2012) Chemical pressure effect on optical properties in multiferroic bulk $BiFeO_3$. J Appl Phys 112:073516
[13] Panwar N, Coondoo I, Tomar A et al (2012) Nanoscale piezoresponse and magnetic studies of multiferroic Co and Pr co-substituted BFO thin films. Mater Res Bull 47:4240–4245
[14] Chung C-F, Lin J-P, Wu J-M (2006) Influence of Mn and Nb dopants on electric properties of chemical-solution-deposited $BiFeO_3$ films. Appl Phys Lett 88:242909
[15] Ederer C, Spaldin NA (2005) Influence of strain and oxygen vacancies on the magnetoelectric properties of multiferroic bismuth ferrite. Phys Rev B 71:224103
[16] Kim YJ, Kim JW, Raghavan CM et al (2013) Enhancement of electrical properties of (Gd, V) co-doped $BiFeO_3$ thin films prepared by chemical solution deposition. Ceram Int 39:S195–S199
[17] Agarwal A, Sanghi S et al (2011) Rietveld analysis, dielectric and magnetic properties of Sr and Ti codoped $BiFeO_3$ multiferroic. J Appl Phys 110:073909
[18] Dong G, Tan G, Luo Y et al (2014) Charge defects and highly enhanced multiferroic properties in Mn and Cu co-doped $BiFeO_3$ thin films. Appl Surf Sci 305:55–61
[19] Wang X, Guangda H, Cheng L et al (2011) Comparative study on aging effect in $BiFeO_3$ thin films substituted at A- and B-sites. Appl Phys Lett 99:262901
[20] Arya GS, Negi NS (2013) Effect of In and Mn co-doping on structural, magnetic and dielectric properties of $BiFeO_3$ nanoparticles. J Phys D Appl Phys 46:095004
[21] Eichel RA, Erhart P, Traskelin P et al (2008) Defect-dipole formation in copper-doped $PbTiO_3$ ferroelectrics. Phys Rev Lett 100:095504
[22] Mao WW, Wang XF, Han YM et al (2014) Effect of Ln (Ln = La, Pr) and Co co-doped on the magnetic and ferroelectric properties of $BiFeO_3$ nanoparticles. J Alloys Compd 584:520–523
[23] Hussain S, Hasanain SK, Jaffari GH et al (2015) Correlation between structure, oxygen content and the multiferroic properties of Sr doped $BiFeO_3$. J Alloys Compd 622:8–16
[24] Ren XB (2004) Large electric-field-induced strain in ferroelectric crystals by point-defect-mediated reversible domain switching. Nat Mater 3:91–94
[25] Yang J-C, Kuo C-Y, Liu H-J et al (2016) Electrically enhanced magnetization in highly strained $BiFeO_3$ films. NPG Asia Mater 8:269
[26] Jin L, Li F, Zhang S (2014) Decoding the fingerprint of ferroelectric loops: comprehension of the material properties and structures. J Am Ceram Soc 97:1–27
[27] Cheng C-J, Kan D, Anbusathaiah V et al (2010) Microstructure-electromechanical property correlations in rare-earth substituted $BiFeO_3$ epitaxial thin films at morphotropic phase boundaries. Appl Phys Lett 97:212905
[28] Yang C, Jiang JS, Qian FZ et al (2010) Effect of Ba doping on magnetic and dielectric properties of nanocrystalline $BiFeO_3$ at room temperature. J Alloys Compd 507:29–32
[29] Wei J, Xue D, Wu CF et al (2008) Enhanced ferromagnetic properties of multiferroic $Bi_{1-x}Sr_xMn_{0.2}Fe_{0.8}O_3$ synthesized by sol-gel process. J Alloys Compd 453:20–23
[30] Xu JL, Xie D, Yin C et al (2014) Mg-doped $Bi_{0.8}Ca_{0.2}FeO_3$ with enhanced ferromagnetic properties. Mater Lett 122:139–142
[31] Srivastav SK, Gajbhiye NS, Banerjee A (2013) Structural transformation and enhancement in magnetic properties of single-phase $Bi_{1-x}Pr_xFeO_3$ nanoparticles. J Appl Phys 113:203917
[32] Park T-J, Papaefthymiou GC, Viescas AJ et al (2007) Size-dependent magnetic properties of single-crystalline multiferroic $BiFeO_3$ nanoparticles. Nano-Lett. 7(3):766–772
[33] Yang KG, Zhang YL, Yang SH et al (2010) Structural, electrical, and magnetic properties of multiferroic $Bi_{1-x}La_xFe_{1-y}Co_yO_3$ thin films. J Appl Phys 107:124109